Modelling compression pressure distribution in fuel cell stacks

Mikko Mikkola [a],[*], Thomas Tingelöf [b], Jari K. Ihonen [b]

[a] *Helsinki University of Technology, Department of Applied Physics, Advanced Energy Systems, P.O. Box 5100, 02015 TKK, Finland*
[b] *VTT, Technical Research Centre of Finland, P.O. Box 1000, FIN-02044, Finland*

ARTICLE INFO

ABSTRACT

A general purpose 3D finite element method model has been developed for the estimation of the compression pressure distribution in fuel cell stacks. The model can be used for the optimisation of any type of fuel cell structure at any temperature. The model was validated with pressure sensitive film measurements using PEFC stack components that had low rigidity and were highly deformable.

© 2009 Elsevier B.V. All rights reserved.

1. Introduction

Uniform compression pressure distribution over the active area and gaskets of the fuel cell stack is essential to its performance and life-time [1] as it has a major impact on the properties of the gas diffusion layer (GDL) and contact resistances [2–10], affecting both current and temperature distributions. The compression pressure is uneven both under the ribs in the flow fields [1,11–13], as well as over the whole membrane electrode assembly (MEA) and gaskets [14–16].

For the low temperature fuel cells the pressure distribution can be measured experimentally near operating temperature using pressure sensitive films. For high temperature fuel cells this is not possible, due to a limited operating temperature range of the pressure sensitive films. Therefore, the compression pressure distribution within a high temperature fuel cell stack must be modelled, which creates a need for an experimentally validated modelling tool. With a high quality modelling tool, optimal end plate structures and clamping schemes of both high and low temperature fuel cells can be readily designed.

In the past a few attempts have been made to simulate the compression pressure within a polymer electrolyte fuel cell (PEFC) using finite element method (FEM) computer models [14,15,21]. Lee et al.

[14] modelled the pressure distribution inside a small unit cell and validated their model with experiments. However, there was up to a 60% difference between model predictions and measurement results, but quantitatively, the trends in results were similar. Liu et al. [15] presented a method to optimise the assembly pressure and clamping bolt locations to achieve more uniform pressure distribution in a unit cell. Their work did not contain experimental validation. Karvonen et al. used a FEM model to investigate pressure distribution in a multicell stack, and compared various end plate structures and materials and clamping force schemes [17]. Their validation process did not include numerical comparison, but qualitatively the results were in agreement. The developed models have shown the importance of correct end plate design and clamping pressure application, but none of them can reliably predict the compression pressure distribution inside a cell or a stack.

The purpose of this work was to develop and validate a widely applicable model that can accurately predict pressure distributions within any type of fuel cell at any temperature. A 3D FEM computer model was developed and validated through experiments with pressure sensitive films using in-house PEFC stack with highly deformable components. Results from validation experiments proved the applicability of the model.

2. Description of the model

2.1. Theory

The equation which is solved in the model is:

$$\nabla \cdot (D\nabla u) = 0 \tag{1}$$

Nomenclature

D	elasticity matrix
E	Young's modulus (Pa)
u	deformation vector
u, v, w	deformation vector components (m)
σ	stress ($N\,m^{-2}$)
v	Poisson's ratio

where D is the elasticity matrix and **u** is the deformation vector consisting of deformations u, v, and w in x-, y- and z-directions, respectively:

$$\mathbf{u} = u\bar{i} + v\bar{j} + w\bar{k} \tag{2}$$

From the solution, stress and strain components can be calculated. In this work, we are mostly interested in the perpendicular stress on stack components. For example, stress σ in the z-direction for isotropic materials can be written as:

$$\sigma_z = \frac{E}{(1+v)(2-v)} \left(v\frac{\partial u}{\partial x} + \frac{\partial v}{\partial y} + (1-v)\frac{\partial w}{\partial z} \right) \tag{3}$$

where E is Young's modulus and v Poisson's ratio. In the case of anisotropic materials, Young's modulus and Poisson's ratio are not constants and thus the elasticity matrix differs from that of the isotropic case. More information on the subject can be found in reference [17] or structural mechanics text books, for example ref. [18].

2.2. Model description

The fuel cell model geometry used in this model is based on an existing fuel cell stack design on which experiments could readily be carried out. The stack structure was simplified for computational and experimental validation purposes by omitting bipolar plates, porous transport layers and gaskets and including only end plates, flexible equalization layers (EQLs), current collectors and bipolar plate substitute. The resulting structure is artificial but still corresponds closely to the situation in the first and last cells in the real stacks, where the compression pressure distribution is usually the most uneven. Further into the stack, the flexibility of cell components makes the pressure distribution more even.

The model is comprised of five separate domains, which were the 40 mm thick end plate, 5 mm thick equalization layer, 10 mm current collector, 1 mm bipolar plate substitute and gas line connector substitutes. The EQL was optional, and was not used in all the modelled cases. The model geometry is shown in Fig. 1. The geometry of each component is identical to the real geometry of the actual stack components except the bipolar plate substitute, which is identical in x–y dimension, but thinner and does not contain flow channels.
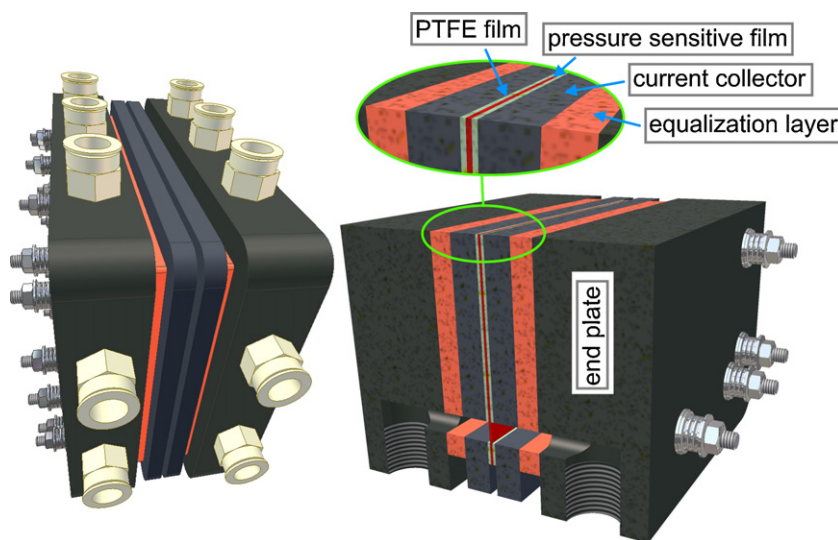

Fig. 1. Left: Stack overview. Right: Stack quarter section view along symmetry planes.

Table 1
Material parameters used in the model.

Component/dimensions	Material	Young's modulus (Pa)	Poisson's ratio	Sources
End plate (130 mm × 96 mm × 40 mm)	Ensigner TECATRON GF40 PPS + 40% glass fibre	13×10^9	0.36	[19]
Current collector (127 mm × 93 mm × 10 mm)	GrafTech GrafCell FFP-300	1.4×10^9	0.25	[20]
EQL (115 mm × 82 mm × 5 mm)	Butyl rubber	7.2×10^6	0.49	Young's modulus measured[a], Poisson's ratio estimated
Bipolar plate substitute (115 mm × 81 mm × 1 mm)	PTFE	0.4×10^9	0.25	COMSOL material library
Gas line fitting substitutes cylindrical, r_1 = 10 mm, r_2 = 7 mm, h = 40 mm	PTFE	0.4×10^9	0.25	COMSOL material library

[a] Measured for 0–12 bar compression using Testometric M500-50 CT universal material tester. The response in that range is linear. The same value has been used for all compression pressures.
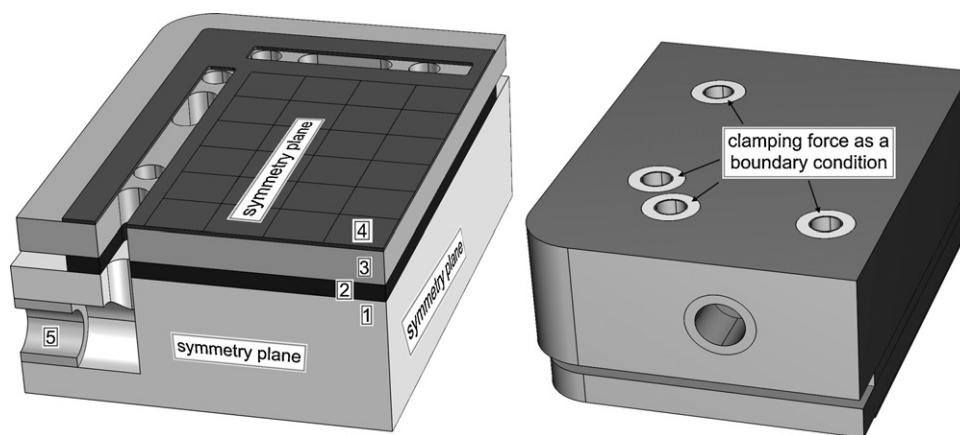
Fig. 2. Left: Model geometry and symmetry planes (1) End plate (2) Equalization layer (3) Current collector (4) Bipolar plate substitute (5) Gas line connector substitute. Right: Areas used for clamping force boundary conditions.

Due to symmetry, the model implements only one eighth of the stack. Symmetry conditions were applied onto all internal section boundaries. A symmetry boundary condition was also applied onto the bottom of the bipolar plate substitute, corresponding to the experimental scenario where the stack is assembled with a thin layer of PTFE in place of bipolar plates. In the model, clamping forces were applied on a washer-shaped area around each bolt hole. The inner and outer diameters were 9 and 16 mm, respectively, giving an area of 1.37×10^{-4} m^2. All other boundaries were free.

Young's modulus and Poisson's ratio were needed for each component to model their deformation under stress. Manufacturer supplied and literature data was used whenever available. Table 1 contains a list of modelled components, their dimensions, materials and material parameters at room temperature, and data sources. All components were assumed isothermal, elastic and isotropic. For the end plate, EQL and bipolar plate substitute isotropy is a reasonably good assumption, but the properties of the current collector material are clearly different in through- and in-plane directions. However, the error caused by the assumption should be insignificant. The deformation of the current collector is minor compared to the EQL and thus, current collector's properties in the in-plane direction have negligible contribution to the resulting pressure distribution.

The model was implemented using COMSOL Multiphysics 3.4, a commercial FEM solver, running on a computer with a dual core AMD Opteron 265 processor, 16 GB of RAM, and GNU/Linux Open-SUSE 10.3 64-bit operating system.

3. Experimental

3.1. Description of the pressure distribution measurement hardware

For the validation measurements, a new metal-free end plate structure was developed for a previously designed in-house stack. The structure included relatively soft end plates made of fibre glass reinforce polyphenylene sulphide (PPS, Ensinger Tecatron GF 40), expanded natural graphite current collectors (GrafTech Graf-Cell FFP-300) and butyl rubber (polyisobutadiene) EQLs. The EQLs between end plates and current collectors deform and thereby transfer pressure from the high pressure regions to the low pressure regions. The developed new end plate structure is metal free. The motivation for the development of the metal-free structure comes from the fact that cations, especially Fe^{2+} and Cu^{2+}, released from any other metal part of the system can act as catalysts for radical formation from H$_2$O$_2$ and also decrease the conductivity of the

membrane [21–24]. Therefore, to maximise polymer fuel cell lifetime it is desirable to eliminate all metallic components in parts of the fuel cell system that are in contact with humidified reactant gas flows.

The experimental set-up is shown in Fig. 2. Between the current collectors a bipolar plate substitute (two 0.5 mm thick PTFE sheets) was added to reduce the disturbing effect of the current collector roughness on the pressure distribution measurements and to avoid discolouration of the pressure sensitive films by the current collectors. Pressure sensitive films (Pressurex® Super Low Pressure LLW, FUJIFILM NDT Systems, Inc.) were placed within the bipolar plate substitute (see Fig. 2). The compression pressure was exerted by a stack of disc springs (Mubea Tellerfedern GmbH) around each clamping bolt.

A set of calibration measurements, in the range of 3–28 bar, were performed to obtain a relation between the colour intensity in the pressure sensitive film and applied pressure. The resulting calibration curve was used in data processing to convert the colour pattern on the pressure sensitive film to numeric pressure distribution data. The applicable pressure range was found to be 4–25 bar.

All experimental work reported here was carried out under controlled ambient conditions. Air temperature and relative humidity were maintained at 23 °C and 50%, respectively. Impact time for all pressure sensitive film measurements was 2 h. All measurements were performed twice.

### 3.2. Test procedure for validation of the computer model

Five test cases (see Table 2) were compiled for model validation. Pressure distribution between the bipolar plate substitutes was both modelled and experimentally measured for all cases. The effect of equalization layer was investigated with three test cases: no equalization layer, basic equalization layer and modified equalization layer. The basic EQL is solid, except for the holes required for clamping bolts and gas channels. The modified, but non-optimised EQL contains additional holes, which modify the overall rigidity in the vicinity of the holes (see Fig. 3). Furthermore, Fig. 3 shows the

Table 2
Test cases for model validation.

EQL	Clamping force arrangement		
	3 kN at each bolt	High forces on short edge	High forces on long edge
No EQL	Case 1		
Basic	Case 2		
Modified	Case 3	Case 4	Case 5
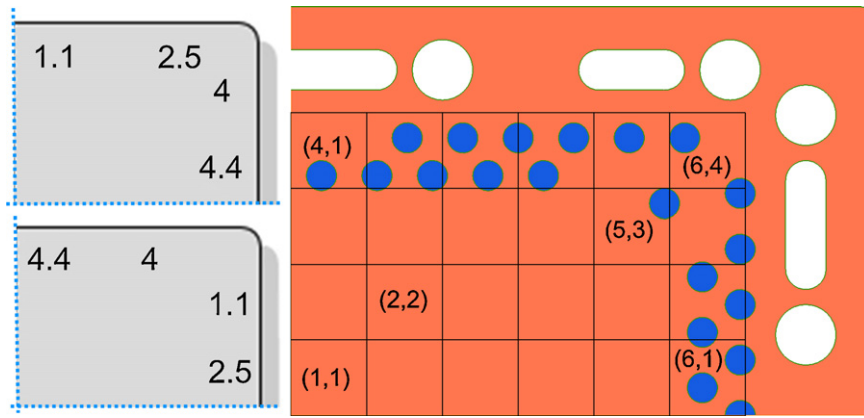
Fig. 3. Left: clamping force cases. Top: Case 4 and bottom: Case 5. Right: equalization layer. The basic EQL does not have the perforations marked with darker colour. Below: the locations of grid squares are given using the coordinate system shown in this figure.
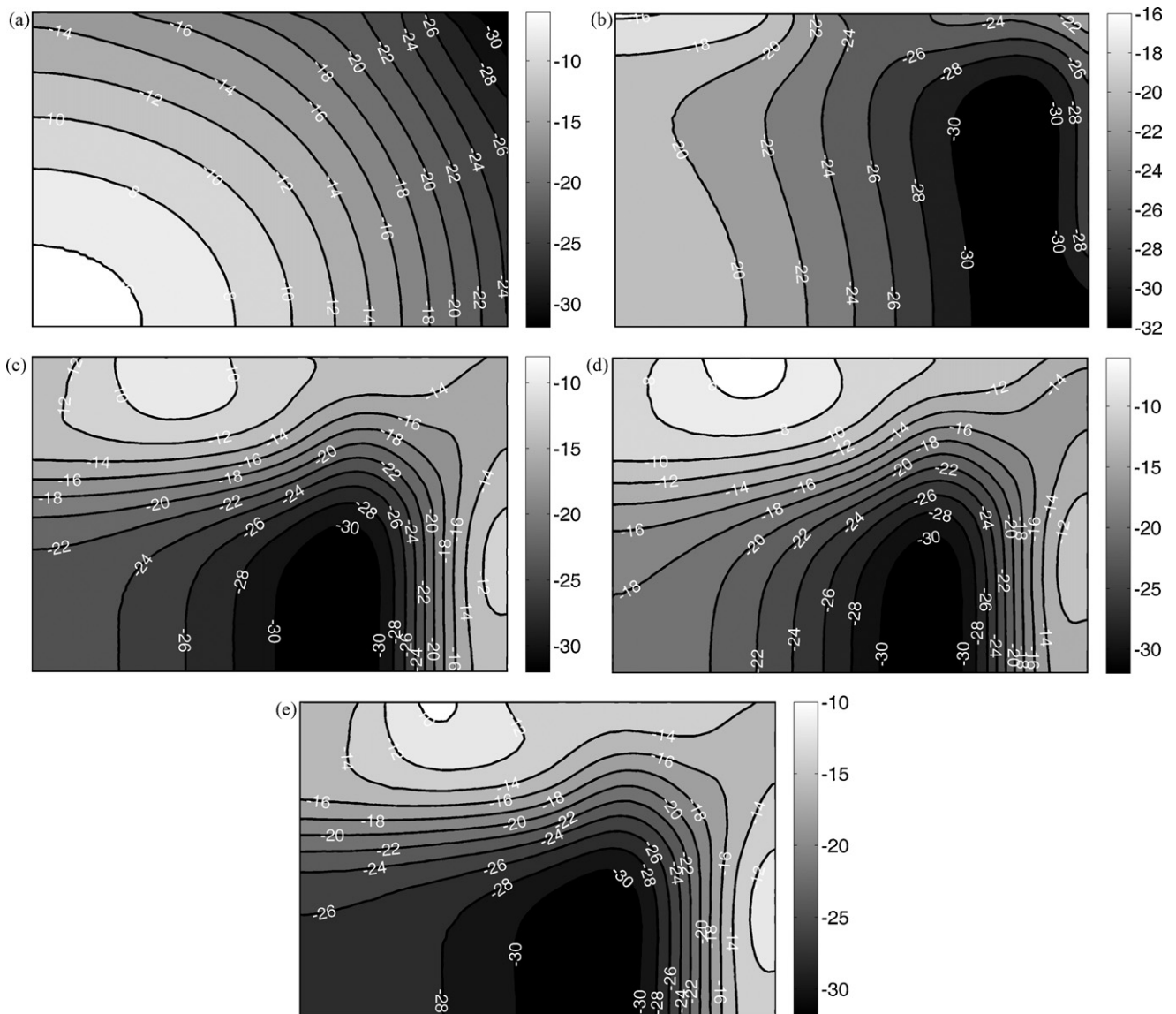
Fig. 4. (a–e) Cases 1–5, respectively. Modelled pressure distributions on the bottom of the bipolar plate substitute over a 90 mm × 60 mm rectangle on the active area. The centre of the stack is at the lower left corner of each picture.

location of 6×4 grid of 15 mm by 15 mm squares, into which the active area was divided. This grid was used in the model validation process.

Three test cases were also used for clamping force distribution. Case 3 is a base case in which 3 kN force was applied to all clamping bolts. In Cases 4 and 5, the majority of the force was applied around the bolts on the short and long edges of the stack, respectively. Clamping forces and their locations can be seen in Fig. 3. In all three cases the total force applied onto one quarter of the end plate is 12 kN. This corresponds to an average pressure of 12.5 bar on the EQL and bipolar plate substitute, which both have an area of ca. 96 cm².

The results from the model and the measured data were analyzed in the following way. Resulting pressure maps were scanned at 300 DPI to digital format and processed using Matlab®. Since the system is symmetric the measured data was averaged over one quarter of the active area in order to get a larger statistical selection. To reduce noise, the data from the scans was further averaged over squares so that the final images had ca. 10^4 data points

The colouration of the pressure maps were converted into surface pressures using the obtained calibration curve. Since data

measured above the saturation limit of the pressure sensitive film cannot be considered reliable all data indicating pressures higher than the saturation limit were set to 25 bar. To analyze the results, the compression pressure over the active area was integrated over the grid squares shown in Fig. 3, and resulting forces were compared between the measurement and modelling results.

4. Results and discussion

4.1. Modelling results

Modelled clamping pressure distributions over the active area are presented in Fig. 4 for different cases given in Table 2. Although the pressure distribution was modelled and measured over the whole area of the bipolar plate substitute, only the distribution on the active area is shown in the figures. In Case 1, there is no EQL present the system to transfer pressure from high pressure regions to low pressure regions and the compression pressure is applied to the outer edges of the active area, especially the outer corner. In Case 2, a solid EQL is applied which compensates for the deformation of the end plate and transfers some pressure from the corners
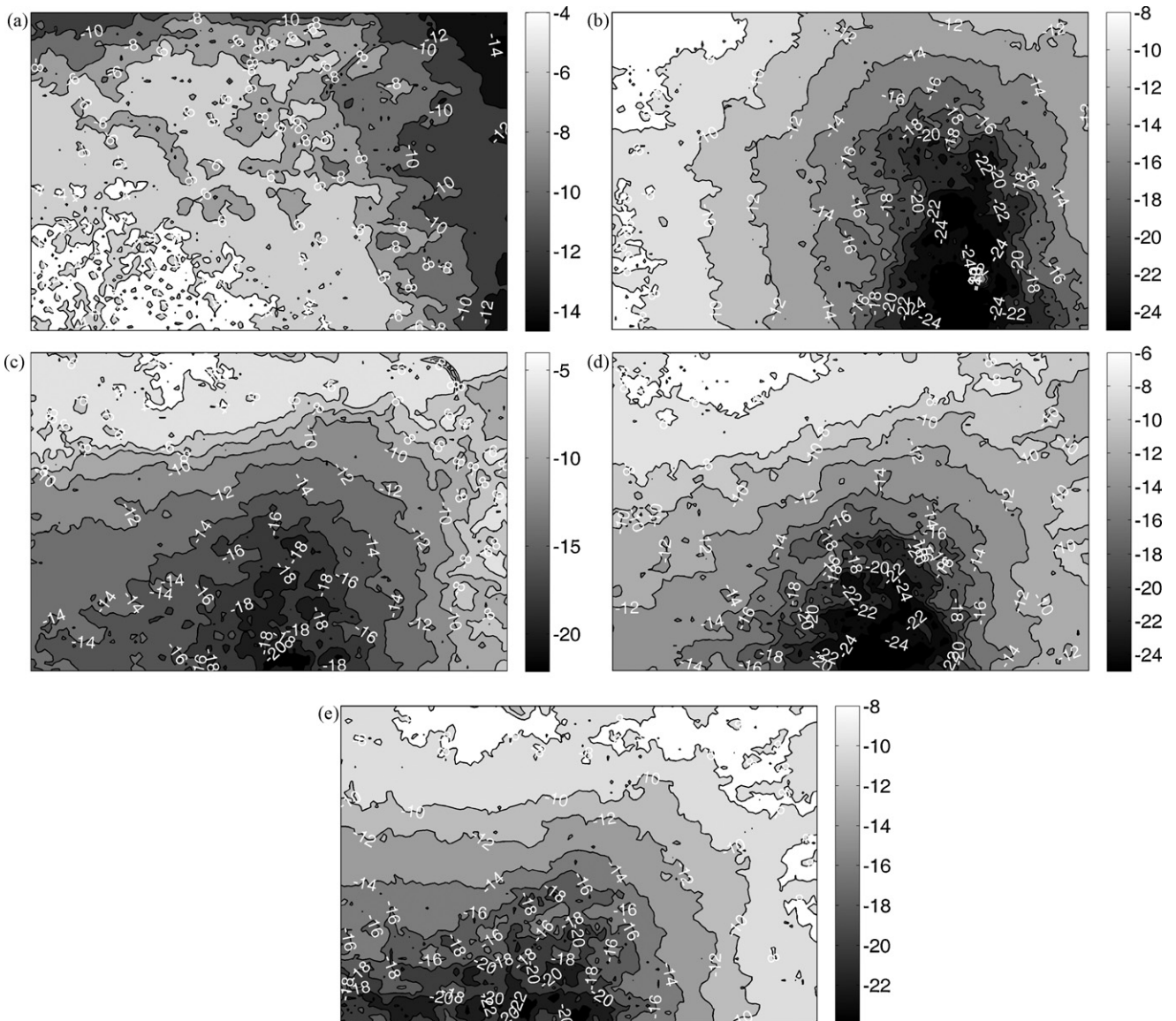
Fig. 5. (a–e) Cases 1–5, respectively. Measured pressure distribution on the bottom of the BPP substitute over a 90 mm × 60 mm rectangle on the active area. The centre of the stack is at the lower left corner of each picture. Top: varying EQL, bottom: varying clamping force scheme. Note the scale in each subpicture.

towards the middle of the active area. In Case 3, an EQL, which is modified for increased deformation, distributes the pressure even more evenly over the active area.

The compression pressure distribution caused by applying different forces to the bolts in the stack was studied with modified EQL. Comparing test Cases 3–5, it can be seen that the clamping force arrangements have a significant impact on the pressure distribution. In Case 5, a significant amount of pressure has been transferred to the middle of the active area due to EQL deformation.

4.2. About numerical solutions

The mesh was automatically generated by Comsol Multiphysics. Mesh element size setting 'Normal' was used for Case 1 and 'Fine' for other cases. The models had from 74 to 175 k tetrahedral mesh elements. Conjugate gradients iterative solver with geometric multigrid preconditioner was used and solution times varied from 15 to 50 min depending on the model. Relative error estimates for nonlinear solver results were on the order of 10^{-15} to 10^{-16}. To investigate the effect of mesh resolution, Case 5 was solved with an alternative mesh consisting of 323 k elements. However, the results were identical to the solution with the coarser mesh.

4.3. Experimental results

Measured pressure distributions for Cases 1–5 are shown in Fig. 5. In all cases, the measured pressure distributions show the same trends as the model predictions. However, there are notable quantitative differences in areas where the measured pressure is close to the upper or lower limit of the pressure sensitive film's range (4–25 bar). Below 4 bar, the pressure does not register on the film, and the colouration reaches saturation at 25 bar. Furthermore, data averaging, which was performed to reduce noise, obscures the areas of highest compression. In general, all measured pressure distributions indicate lower pressures than their modelled counterparts.

4.4. Model validation results

The experimental results in Fig. 5 show the same trends as model predictions presented in Fig. 4. For numerical analysis, the total forces on active areas were determined (see Table 3). Consistently, the model predicts higher compression than the measurements indicate. The most probable cause for this behaviour is the inaccuracy of material parameters used in the model, especially Young's modulus for the current collector and equalization layer.

The correctness of the shape of the modelled pressure distribution was evaluated using the following procedure. First, the pressure for both the modelled and measured results on each grid square was scaled by dividing it by the maximum value in that grid. Then the error between the measured and modelled was calculated using Eq. (4). Error values are presented in Table 4.

$$\text{Error} = 100\% \times (\text{measured} - \text{modelled})/\text{modelled} \qquad (4)$$

The largest errors in each case are seen where the measured pressure was close to the lower end of the measurable range, but where the measured pressure was between 7 and 20 bar, the error is generally below 30%. This confirms that the model predictions are qualitatively correct. Among the cases, the largest errors occur

Table 3
Total compressive force on active area for measured and modelled cases (kN).

|	Case 1	Case 2	Case 3	Case 4	Case 5
Measured	3.70	7.51	5.87	6.57	6.58
Modelled	4.66	8.86	8.59	8.38	8.78

Table 4
The difference between the measured and modelled pressure distributions. The grid coordinates refer to those in Fig. 3.

Grid coordinate	1	2	3	4	5	6
	Case 1					
4	−51.5%	−33.4%	−16.0%	−1.2%	1.4%	0.0%
3	−58.7%	−54.5%	−38.5%	−23.2%	−19.4%	−5.7%
2	−60.1%	−62.3%	−62.6%	−33.9%	−20.9%	−12.7%
1	−58.1%	−58.0%	−58.8%	−33.7%	−13.8%	−16.2%
	Case 2					
4	31.8%	28.5%	28.3%	31.0%	41.5%	48.7%
3	40.7%	25.0%	19.4%	11.2%	24.6%	57.4%
2	29.7%	14.6%	7.7%	4.2%	−0.4%	43.4%
1	27.9%	13.1%	7.2%	−7.0%	−5.8%	31.2%
	Case 3					
4	7.3%	−11.3%	−6.8%	0.7%	23.4%	14.5%
3	−3.2%	−9.6%	−9.4%	3.8%	20.9%	5.0%
2	3.6%	6.8%	4.9%	8.7%	31.5%	−3.3%
1	0.7%	3.5%	1.2%	0.0%	25.2%	−12.1%
	Case 4					
4	−25.7%	−44.8%	−37.6%	−11.7%	2.7%	1.5%
3	−6.1%	−8.2%	−5.1%	16.5%	35.8%	1.5%
2	11.5%	14.0%	9.3%	15.4%	42.8%	−5.6%
1	5.6%	5.9%	−3.7%	0.0%	28.9%	−7.2%
	Case 5					
4	−21.6%	−42.8%	−42.0%	−21.4%	−8.8%	−10.8%
3	−12.9%	−12.0%	−8.2%	10.3%	28.9%	−9.2%
2	2.9%	6.8%	4.8%	25.4%	41.1%	−16.9%
1	−11.4%	−10.4%	−7.8%	15.4%	35.5%	−17.3%

in Case 1, where close to 80% of the compressive force was exerted outside the active area.

4.5. Sensitivity analysis

The model's sensitivity to material parameters was investigated by solving the model for Case 5 using various parameter values and comparing the resulting clamping pressure distribution to the measured one. Young's modulus of the end plate (E_{EP}), equalization layer (E_{EQL}) and current collector (E_{CC}) were varied one at a time from 25% to 175% of the values listed in Table 1. The resulting distributions
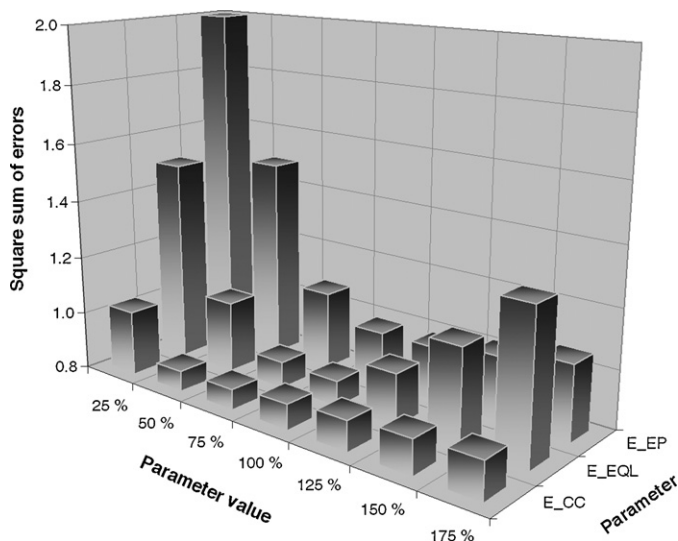
Fig. 6. The model's sensitivity to Young's moduli of the end plate, equalization layer and current collector. The moduli are given in percentage of values in Table 1.

were analyzed by summing the squares of errors (see Eq. (4)) for each parameter value. The parameter value with the corresponding minimum value of the squares sum produced the pressure distribution which resembled the measured one the most. The square sums of errors are presented in Fig. 6. For E_{EP} and E_{EQL} the minimum squares sum was found at 100% of the Table 1 values, but for E_{CC} the minimum was at 50% value. This indicates that the Young's modulus used for the current collector may be inaccurate. Since the error was relatively small and a more reliable value was not available, the estimate for Young's modulus of the current collector was not changed.

5. Conclusions

A FEM-model which predicts the compression pressure distribution and component deformation in the outermost cells in a fuel cell stack has been developed and experimentally validated. It shows good qualitative agreement with measured pressure distributions for different equalization layers, clamping schemes and forces. Quantitatively, the model predicted higher compression pressures than were measured. For a large part, this is due to the limited range of the pressure sensitive film that was used. Here, it was observed that the colour intensity of 5–10% of the pixels in the scans of the pressure sensitive films was at saturation limit. In retrospect, it is clear that several pressure sensitive films with different pressure ranges should be used in experiments to record a larger portion of the pressure spectra.

Other possible sources of error are the uncertainty in some of the material parameters used in the model, and manufacturing tolerances in the experimental hardware. It has been observed that even small errors in component dimensions can cause notable variations in the pressure distribution [14,18]. A preliminary sensitivity analysis was performed to investigate the sensitivity of the model to material parameters.

In the future, the validation process will be developed further, and thermal expansion will be included in the model. This, combined with accurate material property data library, will facilitate predicting compression pressure distribution reliably even at elevated temperatures.

References

[1] I. Nitta, T. Hottinen, O. Himanen, M. Mikkola, J. Power Sources 171 (2007) 26–36.
[2] W. Lee, C. Ho, J.W. Van Zee, M. Murthy, J. Power Sources 84 (1999) 45–51.
[3] J. Ihonen, F. Jaouen, G. Lindbergh, G. Sundholm, Electrochim. Acta 46 (2001) 2899–2911.
[4] C. Lim, C.Y. Wang, J. Power Sources 113 (2003) 145–150.
[5] M. Prasanna, H.Y. Ha, E.A. Cho, S.-A. Hong, I.-H. Oh, J. Power Sources 131 (2004) 147–154.
[6] J. Ihonen, M. Mikkola, G. Lindbergh, J. Electrochem. Soc. 151 (2004) A1152–A1161.
[7] P. Zhou, C.W. Wu, G.J. Ma, J. Power Sources 159 (2006) 1115–1122.
[8] J. Ge, A. Higier, H. Liu, J. Power Sources 159 (2006) 922–927.
[9] W.R. Chang, J.J. Hwang, F.B. Weng, S.H. Chan, J. Power Sources 166 (2007) 149–154.
[10] I. Nitta, O. Himanen, M. Mikkola, Electrochem. Commun. 10 (2008) 47–51.
[11] W. Sun, B.A. Peppley, K. Karan, J. Power Sources 144 (2005) 42–53.
[12] T. Hottinen, O. Himanen, Electrochem. Commun. 9 (2007) 1047–1052.
[13] T. Hottinen, O. Himanen, S. Karvonen, I. Nitta, J. Power Sources 171 (2007) 113–121.
[14] S. Lee, C. Hsu, C. Huang, J. Power Sources 145 (2005) 353–361.
[15] D. Liu, X. Lai, J. Ni, L. Peng, S. Lan, Z. Lin, J. Power Sources 172 (2007) 760–767.
[16] X. Wang, Y. Song, B. Zhang, J. Power Sources 179 (2008) 305–309.
[17] S. Karvonen, T. Hottinen, J. Ihonen, H. Uusalo, J. Fuel Cell Sci. Technol. 5 (2008) 041009.
[18] W.C. Young, R.G. Budynas, Roark's Formulas for Stress and Strain, 7th ed., McGraw-Hill Professional, New York, USA, 2002, p. 832.
[19] Ensinger Ltd. TECATRON GF40. Available at: http://www.ensinger.ltd.uk/docs/datasheets/TECATRON GF 40.pdf (accessed 2008-07-28).
[20] Grafoil data sheet on GrafTech website, http://www.graftechaet.com/upload/GHA sheet properties.pdf (accessed 2005-10-26).
[21] A. Pozio, R.F. Silva, M. De Francesco, L. Giorgi, Electrochim. Acta 48 (2003) 1543–1549.
[22] R. Borup, J. Meyers, B. Pivovar, Y.S. Kim, R. Mukundan, N. Garland, D. Myers, M. Wilson, F. Garzon, D. Wood, P. Zelenay, K. More, K. Stroh, T. Zawodzinski, J. Boncella, J.E. McGrath, M. Inaba, K. Miyatake, M. Hori, K. Ota, Z. Ogumi, S. Miyata, A. Nishikata, Z. Siroma, Y. Uchimoto, K. Yasuda, K.-I. Kimijima, N. Iwashita, Chem. Rev. 107 (2007) 3904–3951.
[23] F.A. de Bruijn, V.A.T. Dam, G.J.M. Janssen, Fuel Cells 8 (2008) 3–22.
[24] W. Schmittinger, A. Vahidi, J. Power Sources 180 (2008) 1–14.